Charged-particle spectra from μ^- capture on Al

A. Gaponenko,[1,*] A. Grossheim,[2] A. Hillairet,[3] G. M. Marshall,[2] R. E. Mischke,[2] and A. Olin[2,†]

[1]*Fermi National Accelerator Laboratory, Batavia, Illinois 60510, USA*

[2]*TRIUMF, Vancouver, British Columbia, Canada V6T 2A3*

[3]*Department of Physics and Astronomy, University of Victoria, Victoria, British Columbia, Canada V8P 5C2*

(Received 20 August 2019; revised manuscript received 13 December 2019; accepted 10 February 2020; published 13 March 2020)

Published data on the emission of charged particles following nuclear muon capture are extremely limited. In addition to its interest as a probe of the nuclear response, these data are important for the design of some current searches for lepton flavor violation. This work presents momentum spectra of protons and deuterons following μ^- capture in aluminum. It is the first measurement of a muon capture process performed with a tracking spectrometer. A precision of better than 10% over the momentum range of 100–190 MeV/c for protons is obtained; for deuterons of 145–250 MeV/c the precision is better than 20%. The observed partial yield of protons with emission momenta above 80 MeV/c (kinetic energy 3.4 MeV) is $0.0322 \pm 0.0007(\text{stat}) \pm 0.0022(\text{syst})$ per capture, and for deuterons above 130 MeV/c (4.5 MeV) it is $0.0122 \pm 0.0009(\text{stat}) \pm 0.0006(\text{syst})$. Extrapolating to total yields gives $0.045 \pm 0.001(\text{stat}) \pm 0.003(\text{syst}) \pm 0.001(\text{extrapolation})$ per capture for protons and $0.018 \pm 0.001(\text{stat}) \pm 0.001(\text{syst}) \pm 0.002(\text{extrapolation})$ for deuterons, which are the most precise measurements of these quantities to date.

DOI: 10.1103/PhysRevC.101.035502

I. INTRODUCTION

When a negative muon loses energy by ionization and scattering in matter it encounters the field of the nucleus and at kinetic energies below the order of 10–100 eV it can undergo atomic muon capture [1,2] forming a bound muon-nucleus state, a muonic atom. The μ^- in the muonic atom will typically reach the lowest 1S energy level. The weak interaction of the bound muon with the nucleus leads to nuclear muon capture $\mu^- + (Z, A) \rightarrow \nu_\mu + X$ competing with muon decay. Here X is a final state consisting of a residual nucleus and perhaps one or more protons, neutrons, γ's, etc., [3]. In this paper "muon capture" refers to nuclear muon capture.

Muon capture and neutrino-nucleus interaction are closely related processes. The capture process probes nuclear response in the energy range below 100 MeV, providing a valuable validation of theoretical models of importance to current and future neutrino experiments [4,5]. Upcoming Mu2e [6] and COMET [7] experiments will stop intense negative muon beams in aluminum to look for charged lepton flavor violation. About 61% of the muons will undergo the nuclear capture process. Secondaries from the capture will create unwanted detector rates. In particular, protons and deuterons from capture are highly ionizing and can deaden the tracker. It is important to understand their rates to optimize the detectors. There is an ongoing joint effort between Mu2e and COMET to study muon capture on aluminum in a dedicated AlCap experiment [8]. The present analysis, on the other hand, uses an opportunistic μ^- data set acquired by the TRIUMF Weak Interaction Symmetry Test (TWIST) experiment [9,10]. The same data were previously analyzed for the electron spectrum from muon decay in orbit (DIO) [11].

A theoretical model to describe the yield and spectrum of protons from muon capture was developed by Lifshitz and Singer [12,13]. It considers both preequilibrium and compound-nucleus emission from the excited nucleus with only 7% of the yield from the preequilibrium phase for muon capture on Al. The agreement between the results of these models and data available at that time was reasonably good. The predicted yield for proton emission (plus any number of neutrons) is 4.0% per capture and the corresponding yield for deuterons is 1.2%. For the highest-energy part of the spectrum, the impulse approximation is inadequate and capture on pairs of nucleons must be included [14].

Published data on the emission of charged particles from nuclear muon capture come from several types of experiments. Studies with photographic emulsions [15–17] provide information on both the spectrum and the yield of charged particles, but are limited in their choice of the target nucleus. Another spectrum measurement with an active target was done by stopping negative muons in a silicon detector [18].

*gandr@fnal.gov

†Affiliated with: University of Victoria, Victoria, British Columbia, Canada.

Measurements with external scintillator calorimeters were done for multiple elemental targets, see Refs. [19,20] and references therein. However, they were only able to detect a small high-energy tail of the charged particle spectrum, with the bulk of the spectrum being below the detector threshold. (Note that the proton spectrum in, for example [18], peaks at 2.5 MeV, and a proton at this energy has a range of only dozens of microns in material.) Another class of experiments measures radioisotope production after irradiating a target with negative muons [21,22]. Those experiments allow to deduce the total amount of charged particles emitted in the capture process, but do not provide any information on their spectra, and can not differentiate reaction channels that produce the same final-state nucleus. (For example emission of p and n versus emission of a deuteron.) The present work is the first observation of the momentum spectra of charged particles from muon capture in a magnetic spectrometer, and it is subject to different systematic uncertainties than calorimetric energy spectra measurements in earlier experiments and in AlCap.

In the absence of data about most of the spectrum of protons from muon capture on Al, the experimental spectrum of charged particles from muon capture on Si [18] was parameterized by Hungerford [23] for the MECO proposal [24]. From the (sometimes contradictory) literature Hungerford estimated the per capture rate for protons to be 10%, and approximated the spectrum as

$$W_H(T) = A(1 - T_{th}/T)^{\alpha} e^{-T/T_0} \quad (1)$$

for kinetic energy of the proton $T < 8$ MeV, and as a pure exponent in kinetic energy with different slopes below and above 20 MeV [23]. Although some versions of GEANT 4 [25] include code to generate charged particle emission after muon capture, the empirical spectrum from Ref. [23] has been used as a practical solution for simulations of the energy spectrum of protons from muon capture by both Mu2e and COMET experiments that succeeded MECO.

II. EXPERIMENTAL SETUP

The TWIST detector (Fig. 1) has been described in detail in earlier publications, see Refs. [26,27]. In this section, components that are of particular interest for this analysis will be discussed. The muon beam line was configured to transport a negative beam of approximately 29 MeV/c with about 1% momentum bite. The incoming beam contained cloud muons (negative muons generated in the proximity of the production target) at a rate of 80 Hz. A thin plastic scintillator at the upstream end of the spectrometer provided a trigger signal, with a threshold chosen to be mostly insensitive to electrons that dominated the beam flux. The trigger was unbiased for muon decay or capture products.

The muons were then transported into the center of the detector and stopped in a 71 μm thick 99.999% pure Al target. The muon range was adjusted using a gas degrader controlled by a feedback loop. Two stacks of 22 high-precision planar drift chambers (DCs) were located upstream and downstream of the target. In addition, a total of eight multiwire proportional chambers (PCs) were placed at the very upstream

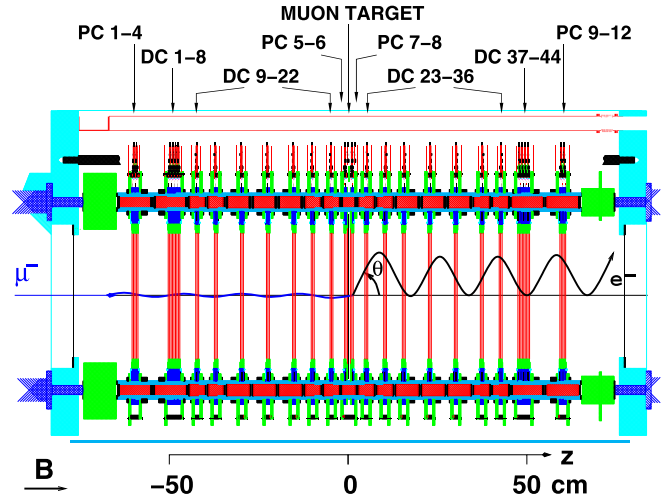

FIG. 1. A cross section of the TWIST detector array, including an example μ^- decay event.

and downstream ends of the detector to support the event reconstruction by providing timing information. The target was surrounded by another four PCs (PC5,6 upstream and PC7,8 downstream) to enable the measurement of the stopping position of each individual muon. The target itself served as the cathode foil of the two innermost PCs; thus the gas volumes surrounding the target were sensitive. A DC consisted of 80 sense wires at 4 mm pitch surrounded by 6 μm thick aluminized Mylar cathode foils separated by 4 mm, filled with dimethyl ether at atmospheric pressure. Most DCs were paired into modules of two (so-called u and v modules) with the central foil shared. A relative rotation of the wire planes by 90 degrees allowed for the reconstruction of the position of a hit in the perpendicular plane. The PCs were of similar design, but their wire planes were equipped with wires at 2 mm pitch and a faster gas (80:20 mixture of CF_4 and isobutane at atmospheric pressure) was chosen. Charge collection time in the PCs was faster than 100 ns, while in the DCs it could exceed 1 μs. In addition to the leading edge time, the time-over-threshold was recorded as an estimate of the size of the signal, approximately proportional to the energy deposit. The gains of PCs 5 and 6 were reduced to avoid saturation of the signal for slow muons; this reduced their detection efficiency for electrons drastically. However, these PCs could then be used to select muons that stopped in the Al target rather than the PC6 gas. The space between the chambers was filled with a (97:3) mixture of helium and nitrogen. The complete detector was contained in a superconducting solenoid magnet, providing a highly uniform field of 2 Tesla.

III. MONTE CARLO SIMULATION

The Monte Carlo simulation (MC) of the experiment that was developed for previous TWIST measurements was adapted for this analysis. It contains a detailed description of the geometry of the detector and the response of its components to particles traversing the detector [10,27]. The MC is implemented in GEANT 3.21 [28]. Its output is in the same

format as the detector data and is processed by the same reconstruction program. The simulation was carefully validated by extensive comparisons with data [10,29]. The accuracy of the geometric description and the amount of material in the detector are of particular importance to the current analysis. Earlier TWIST studies did not cover the passage of protons and heavier particles emitted in the muon capture process through detector material. We use out-of-the-box GEANT 3.21 description of such processes for this analysis, and assess a resulting systematic uncertainty based on agreement with our data, as described in Sec. V D.

The simulation starts with a muon entering the detector. (Beam electrons and pileup muons are also simulated with appropriate rates.) The muon is tracked through the detector with all its GEANT 3 interactions enabled. Typically it ranges out and stops in detector material, at which point a custom routine is called to produce a capture proton, deuteron, etc., or a decay in orbit electron. The daughter particle is subsequently tracked through the detector with all its interactions enabled.

The muon beam momentum and momentum bite affect the muon stopping distribution inside the target. That distribution is expected to have a significant effect on the spectra of capture protons and deuterons exiting the target, because the 71 μm foil is thick compared to the range of a few-MeV proton in aluminum. A procedure based on matching MC distribution of last wire plane hit by the incoming muon to data [10] was used to tune μ^- beam parameters in the simulation. The GEANT 3 code does not include the physics of the muon atomic cascade, which affects the last hit plane distribution due to electromagnetic secondaries escaping the target. A GEANT 4 version 10.2 MC [25,30,31] was used to estimate the effect and derive the corrections of -39.4 keV/c to MC beam momentum and -37.8 keV/c to the momentum bite width. Applying the correction shifted the mean muon stopping position by $(-1.5 \pm 0.1)\,\mu$m, and the final uncertainty on the matching between data and MC is $\pm 2\,\mu$m as documented in Ref. [10]. The muon stopping distribution is further discussed in Secs. IV A and V.

Simulated samples of protons and deuterons from muon capture are only used in this analysis to obtain the detector response function (defined in Sec. IV E). Therefore, a particular distribution of simulated protons or deuterons in momentum is not important as long as it covers a sufficient kinematic range. An exponential distribution in kinetic energy $f(E_k) = \exp[-E_k/(5\text{ MeV})]$ was used for both types of particles. The analysis also uses samples of electrons from muon decay in orbit (DIO), and triton and α particles from muon capture. The shape of the DIO distribution is taken from [11], and shapes of triton and alpha distributions are extracted from a GEANT 4 version 10.2p03 simulation of muon capture on aluminum that used the GEANT 4 precompound model [32]. Technically the default constructed `muMinusCaptureAtRest` process for the negative muon is replaced in our simulations with a new `G4MuonMinusCapture` instance that is given a `G4MuMinusCapturePrecompound` argument. The precompound model is expected to be more accurate (Ref. [33], Sec. 4.1) than the Bertini model used in that GEANT 4 version by default.

IV. ANALYSIS

The objective of the analysis is to determine detector-independent normalized spectra for protons and deuterons from muon capture. The approach is to select a sample of events where a trigger muon stopped in the target and produced a delayed track, and reconstruct these tracks. Positive tracks are protons and heavier particles emitted after muon nuclear capture, and are the main subject of this analysis. Reconstructed distributions of positive tracks from data are corrected for detector efficiency and resolution effects, which are extracted from MC, as described in Sec. IV E and the Appendix. Negative tracks are due to DIO electrons, and are used to determine the absolute normalization of the result, Sec. IV D.

The same event selection and reconstruction is applied to real detector data and MC. A single exception in treating data and MC in the same way is not using a cross talk removal algorithm on MC events, because electronic cross talk was not simulated. This is further discussed in Sec. V.

A. Event selection

The data set considered for this analysis contains 57×10^6 triggered events. After removal of most crosstalk hits, the hits are grouped by time. The prompt time window included hits belonging to the incident muon. A separate window starting at 400 ns included hits corresponding to muon decay or capture products. The start of the delayed time window was a compromise between the time required to collect all ionization from the DC cells (up to 1000 ns) and the effective muon lifetime in Al (864 ns [11]). Requiring wire plane hits up to the stopping target and no hits downstream of the target in the time window corresponding to the trigger time, and demanding the radial position of the stopped muon to be within 2.5 cm of the detector center, yields 22×10^6 events. Most of those events are due to muons stopping in the target, but that signature is also consistent with stops in gas or wires of PC6, and such stops comprise about 9% the sample at this selection stage. Out of target stops are suppressed by a cut that uses hit time-over-threshold measurements in PC5 and PC6 as proxy for muon energy deposition [27,34]. The cut suppresses out of target stops to below 0.5%, which is negligible for the present analysis. It also carves the muon stopping distribution inside the target as shown by the MC simulation in Fig. 2. (The quasiperiodic bump structure in the figure, as well as in Figs. 7 and 8 below, is an artifact caused by an interplay of three different discretizations: single precision floating point numbers in GEANT 3, packing of real numbers into integers in TWIST data format, and the bin size of the final histogram.) The number of events passing the cut is 18×10^6.

Further selection identifies events with charged particles from muon capture or decay. For this analysis, only the downstream chambers were used for measuring decay or capture tracks to avoid complications from the reduced gain of PCs 5 and 6. Also, hits from downstream decay or capture tracks are not affected by leftover gas ionization from the incoming muon. A delayed hit is required in one of downstream PCs 7–12, and beam pileup as identified by PC1–PC4 is vetoed

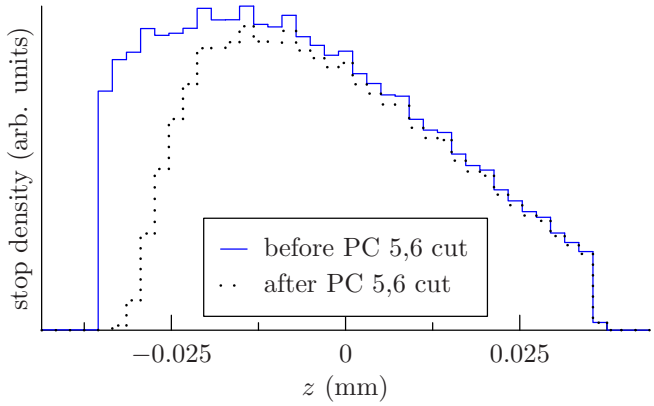

FIG. 2. Simulated distribution of muons stopping in the Al target before (solid) and after (dotted) the cut to eliminate stops in PC6 gas and wires.

in the delayed time window. Then timing cuts on the delayed time window with respect to the trigger particle and possible pileup particles are applied. This selection leaves 2.4×10^6 downstream candidate events. The efficiency of cuts up to this point is the same for DIO and reconstructable capture tracks, which reduces systematic uncertainty on the normalization.

B. Reconstruction of positively charged tracks from muon capture

Sophisticated track finding and fitting software had been developed to reconstruct muon decay tracks in the TWIST detector [10]. It was modified for this analysis to optimize its performance for proton tracks from muon nuclear capture. Protons have higher momentum than muon decay positrons, and some are not radially contained in the detector. This leads to many tracks having fewer hits for track finding compared to the positron case. Low energy protons range out in the detector material, and also have only a few hits. These effects motivated the inclusion of PC hit information in the track finding code for the present analysis.

For the original TWIST analysis the positron trajectories were first fit to the wire centers of the hits, and then the track was refined using drift times. Because our drift time correction was only valid for relativistic particles, we chose to use only the wire center fits, as this gave adequate resolution. Energy loss and multiple scattering in the detector materials are incorporated in TWIST fits [10]. For this work the values were changed to ones appropriate for protons.

Fiducial cuts are made to include only tracks that can be reconstructed reliably with adequate resolution. Thus tracks must have $0.5 < \cos(\theta) < 0.98$, $p_t > 11.9$ MeV/c, and $p_z > 28.4$ MeV/c. Here θ is the angle between the detector axis pointing downstream and the initial momentum direction of the particle. The transverse distance between the position of the stopped muon and the extrapolation of the track to the target plane is required to be less than 1.5 cm. The number of events with positive tracks passing all the cuts is 22.3×10^3.

The RMS momentum resolution of reconstructed proton tracks is better than 8% between 100 MeV/c and 200 MeV/c.

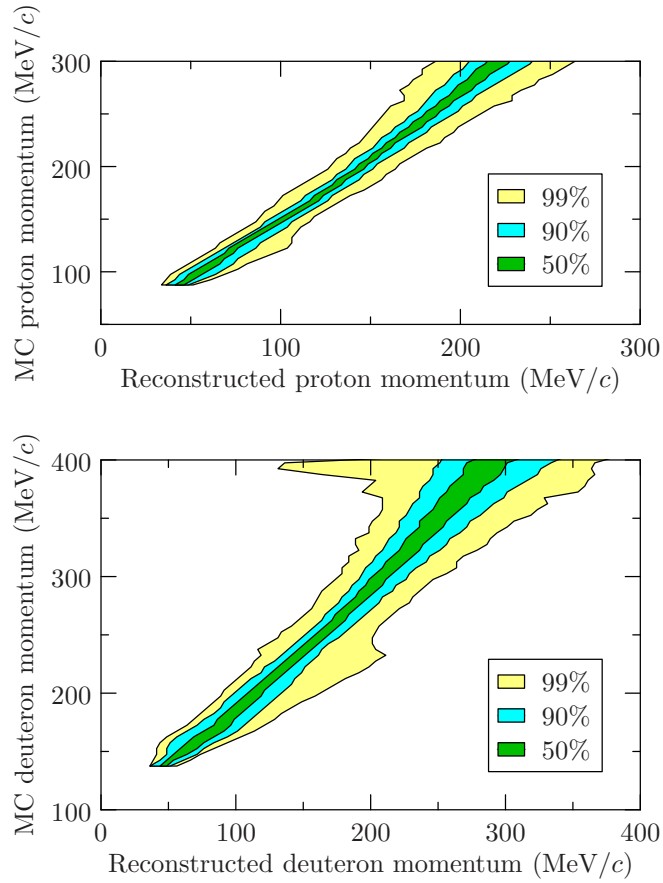

FIG. 3. Track momentum resolution for protos and deuterons. For a fixed true particle momentum at the production vertex (the vertical axis), there is a distribution of reconstructed momenta (the horizontal axis). The contours show the shortest horizontal intervals that contain a given fraction of reconstructed tracks for each true momentum.

For deuterons it is better than 15% between 150 MeV/c and 300 MeV/c. Momentum resolution is illustrated in Fig. 3. One can notice that the most probable value of reconstructed momentum is different from its MC truth value. As the intent was to use unfolding to correct for both resolution and energy loss effects, we did not attempt to tune out the difference at the track reconstruction stage. The product of reconstruction efficiency and acceptance for protons and deuterons based on MC is shown in solid lines in Fig. 4.

C. Separation of protons and deuterons

The probability of events being protons or deuterons is based on the difference of range in material vs momentum relationship between protons and deuterons. A subset of events where the track ranges out in the detector material (contained sample) is identified by requiring that the helical extrapolation of the track starting at the target does not exit the instrumented part of the detector radially, and that the range of DC planes hit by the particle ends at or before the last downstream DC. The cut was based on just DC chambers because of a higher noise level observed in the outer PCs. The range of

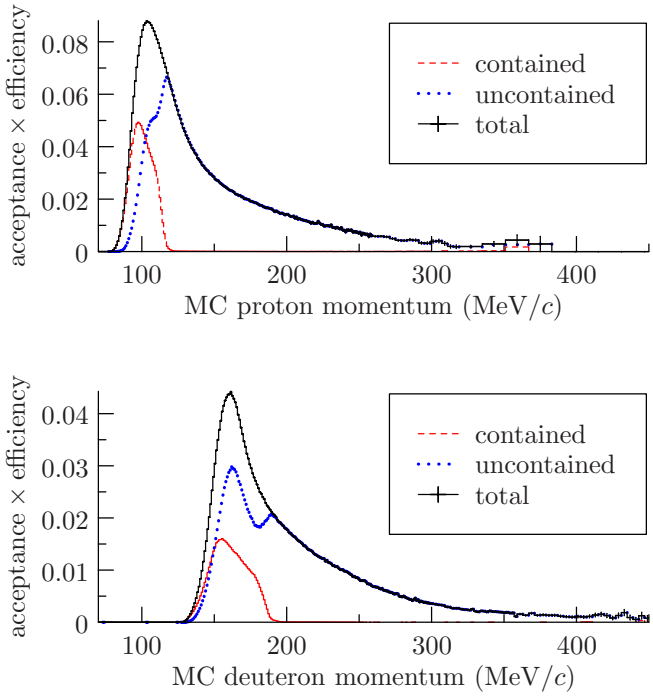

FIG. 4. Reconstruction efficiency times acceptance vs momentum for protons (top) and deuterons (bottom) estimated from MC. The denominator includes all tracks emitted by muons captured in the stopping target. Contained and uncontained subsamples are discussed in Sec. IV C.

planes hit by the particle was defined to start at the stopping target and include all planes with hits on the fitted track, as well as adjacent downstream planes with contiguous hits in the track time window. The adjacent planes were included to account for the fact that our tracking drops hits at the end of particle range, because in that region the trajectory is dominated by random scattering and the hits do not contribute information about the track initial kinematic. In the TWIST planar detector geometry the amount of material traversed by a particle that crosses a detector layer is proportional to $1/|\cos(\theta)|$. Therefore the number of planes (DCs and target PCs) traversed by a track was divided by $|\cos(\theta)|$ and used as the track range variable $\mathfrak{R}$. A distribution of track range vs momentum in data is shown in Fig. 5(a). MC generated plots for protons and deuterons separately are shown in Figs. 5(b) and 5(c).

Tracks that are not contained provide information about the momentum distribution of events and are combined with the contained sample in the likelihood function used in the analysis, as described in the Appendix. Figure 6 shows the reconstructed momentum spectrum of positive tracks in data for both contained and uncontained samples.

D. DIO normalization

Both the electron spectrum and TWIST detector response to it are known with high precision [11], which allows us to use reconstructed negative tracks to determine the number of muon decays in the selected sample of events. The ratio of

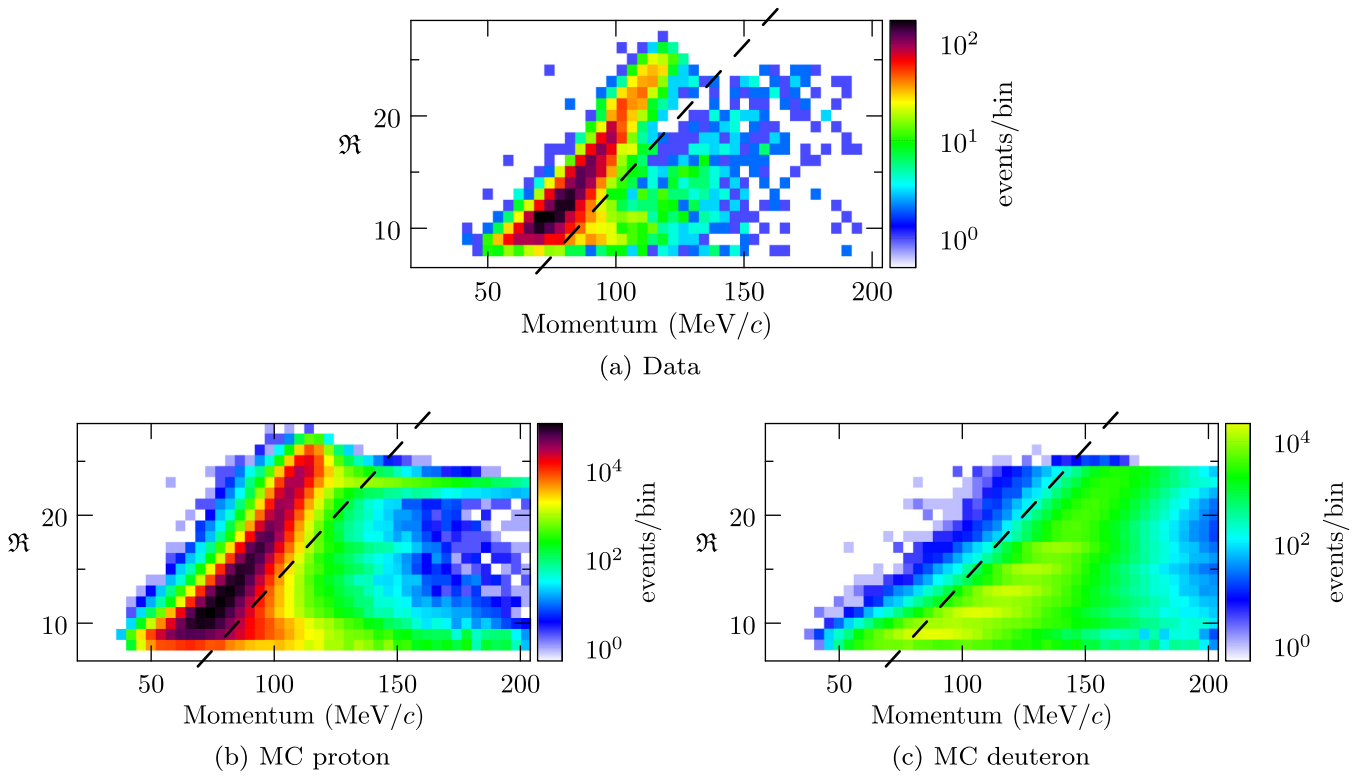

FIG. 5. Range $\mathfrak{R}$ vs reconstructed momentum spectra for contained tracks in data and MC. The dashed line is a guide to the eye to indicate proton-deuteron separation; it is not used in the analysis.

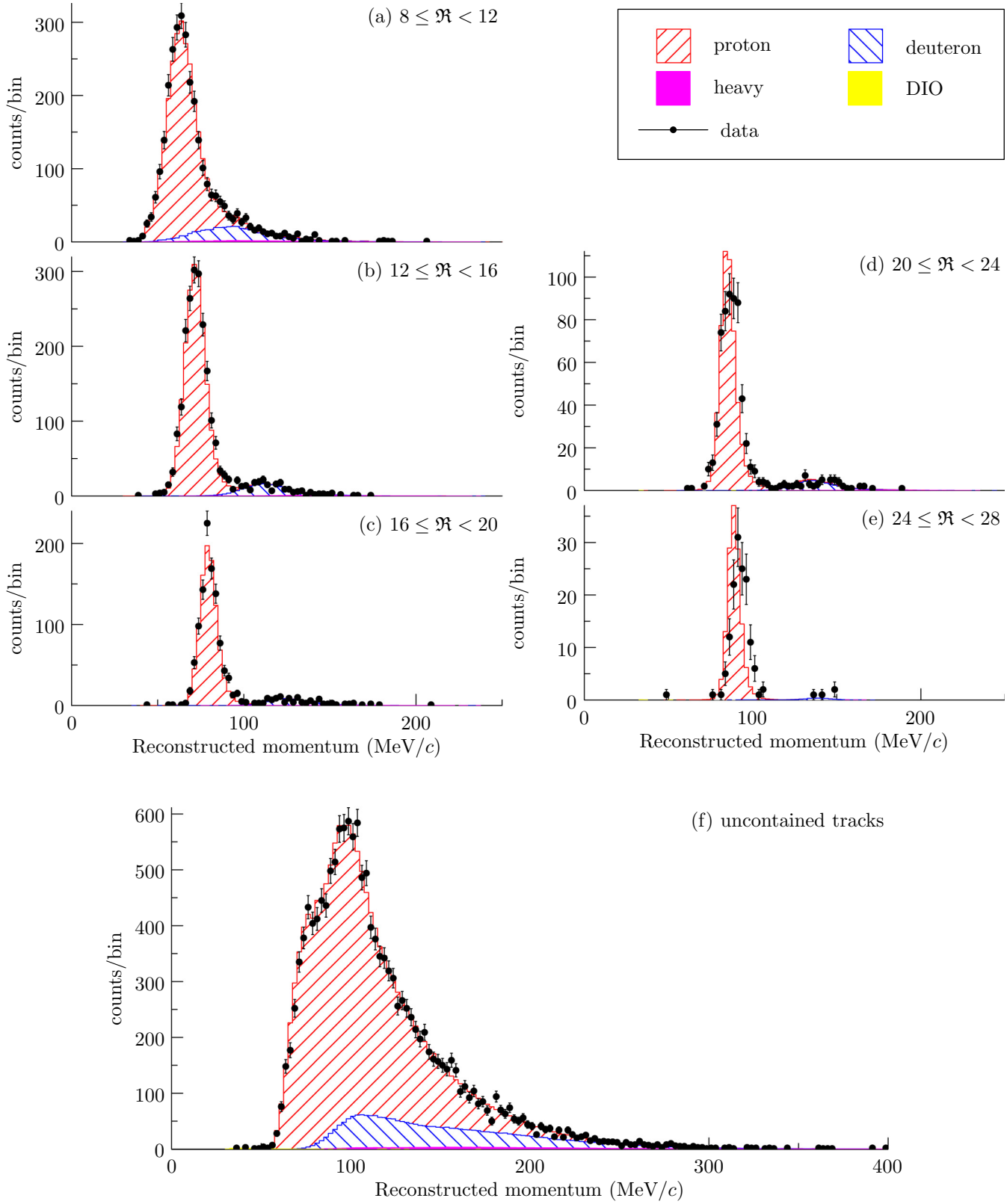

FIG. 6. Reconstructed momentum in slices of track range, and stacked simulation distributions after fit to data.

muon capture events to DIO in Al has been measured to be 0.609:0.391, with an uncertainty of 0.001 [35], therefore a per-capture normalization for the positive track sample can be determined from reconstructed negative tracks.

Only downstream muon decays are counted in this analysis. This provides almost 0.7×10^6 DIO events for the normalization sample, rendering the statistical uncertainty negligible. The sample is known to be unpolarized [11].

The advantage of using DIO tracks for normalization is that efficiencies of cuts that deal with muon preselection or pileup particles are identical for muon capture and decay events, providing data-to-data and MC-to-MC cancellations in the normalization, without requiring to match absolute cut efficiencies in data and MC.

E. Unfolding

The extraction of the desired physics result, truth level proton, and deuteron momentum spectra, from experimentally measured quantities that are smeared by the detector resolution is called unfolding. The unfolding problem is known to be ill-posed: truth level spectra that are significantly different from each other can map into detector distributions that have only infinitesimally small differences [36–39]. It has been shown that approximate solutions to unfolding problems can be obtained by using a regularization procedure [40–42], which reduces the variance of the result at the price of introducing a bias.

In this study, the data observables are the histogram bin contents in the exclusive contained and uncontained channels. Figures 6(a)–6(e) show the momentum spectrum of the contained tracks in slices of the track range variable $\mathfrak{R}$ (defined in Sec. IV C). Figure 6(f) shows the spectrum of uncontained tracks.

Our initial attempts using a maximum likelihood fit to data with standard regularization procedures consistently produced unphysical rising behavior of the result at the high momentum end of the unfolding range, no matter where the end of the range was defined. The resulting curve would contain the true spectrum within its uncertainty band and thus be technically valid, however, it is desirable to present a physically plausible curve as the central value result. There were two factors that caused the rise at the end: one was the contribution of the overflow region, i.e., the part of the spectrum above the unfolding cutoff. The second factor was the bias from the unfolding regularization term. The high momentum region has small data statistics, and is therefore more susceptible to the bias.

We addressed both of those issues by utilizing a novel unfolding method [43], which tunes the existing mathematical apparatus of unfolding to our specific task. In this approach we treat momentum spectra of interest as arbitrary functions below an unfolding cutoff, and physically motivated exponentials in kinetic energy above the cutoff, with parameters of the exponents included in the fit. The continuation of the solution with a parametrized function outside of the unfolding region provides a correct handling of the overflow region contribution. Another key idea is to impose regularization not on the complete physics spectrum, but on just the arbitrary function part of it, with the overall exponential behavior factored out. Then a regularization term that biases its spectrum to a constant will bias the final physics spectrum towards the exponential shape, which is a better approximation for the low statistics region than a constant or a straight line. The Appendix provides more technical details on the unfolding procedure.

The unfolding accounted for two sources of background: contribution of heavier than deuteron particles emitted in muon capture (tritons and α's), and DIO electrons misreconstructed as positive tracks. The shape of each of the two backgrounds was taken from the simulation described in Sec. III, while the two normalizations were free fit parameters.

In addition to data, Fig. 6 also shows fitted contributions from different processes. Fit component yields are 19.1×10^3 protons, 2.9×10^3 deuterons, 250 heavier than deuteron particles, and 12 misreconstructed DIO events for the 22.3×10^3 sample of data tracks. The fit agreement with data is excellent for the uncontained spectrum, and is good for most bins of the contained spectrum. There is a discrepancy for longer-range tracks, clearly visible in Fig. 6(e). The peak in the reconstructed MC track momentum distribution is shifted down compared to the data peak by about 3%. This is further discussed in Sec. V D. Unfolded proton and deuteron spectra are shown below in Figs. 11 and 12 in Sec. VI.

TABLE I. Statistical and systematic uncertainties on partial yield of protons and deuterons per muon capture on Al.

Uncertainty	proton	deuteron
Crosstalk	0.00205	0.00018
Stopping position	0.00010	0.00001
Stopping distribution	0.00049	0.00020
Energy loss	0.00025	0.00032
Background	0.00004	0.00036
Unfolding procedure	0.00032	0.00026
Combined systematic	0.00215	0.00061
Data statistics	0.00066	0.00088
MC statistics	0.00006	0.00009
Total	0.00225	0.00108

V. SYSTEMATIC UNCERTAINTIES

A discrepancy between the simulation of an effect and its actual impact on data would introduce a systematic error in the result. Systematic uncertainties are estimates of the size of such errors. In this study they are typically evaluated by modifying a parameter in simulation and measuring the effect on the resulting yields and spectra by performing the complete unfolding procedure with the modified sample. Another source of systematic error is the unfolding bias. It is estimated by performing unfolding of data with baseline MC samples while modifying some of the settings in the procedure. The rest of this section provides details on individual uncertainties, and Table I gives a summary of their effects on the measured yield of protons and deuterons. Figures 11 and 12 in Sec. VI show the momentum-dependent total uncertainty of

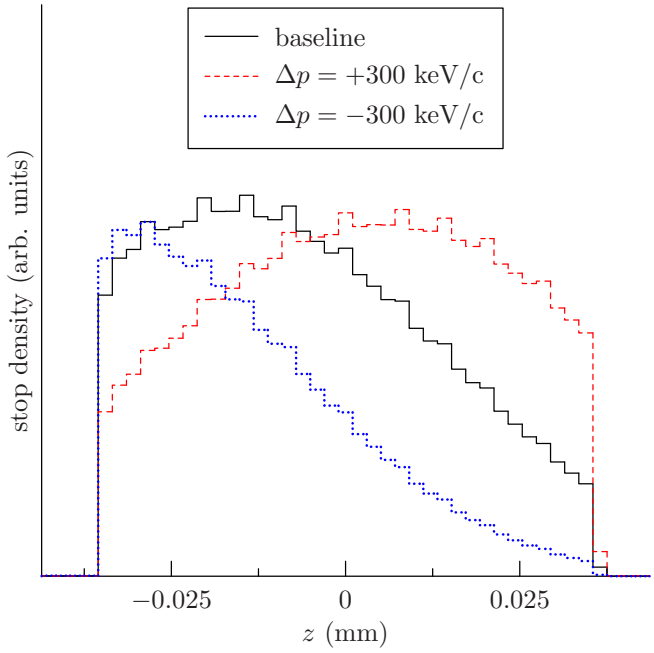

FIG. 7. Simulated distribution of muons stopping in the Al target for the baseline and modified beam momentum samples.

the unfolded spectra, which includes a quadratic sum of all the systematic uncertainties discussed in Secs. V A–V F below.

Among systematic uncertainties the most important ones for proton are cross talk (below 200 MeV/c) and unfolding procedure (above 200 MeV/c). For deuteron, the energy loss systematic dominates in most of the momentum range below 300 MeV/c, and cross talk and heavy particle background uncertainties become dominant above 300 MeV/c.

A. Muon stopping position

The muon beam momentum in the baseline simulation was tuned as described in Sec. III, resulting in a ± 2 μm uncertainty on the stopped muon position. Modified simulation samples were produced by changing the beam momentum by ± 300 keV/c. The resulting shifts in the stopped muon distribution are shown in Fig. 7. The 300 keV/c momentum modification shifted the peak position by about 10 times the uncertainty. The stopping position systematic uncertainty was evaluated by taking the difference between data unfolding results with the $+300$ keV/c sample and -300 keV/c sample, and scaling it down by a factor of 20. Although the simulation samples were produced by modifying the beam momentum, this systematic uncertainty also covers other effects that shift the stopping distribution, such as differences in the amount of material in the muon path between data and MC and simulation of muon dE/dx.

B. Carving of the muon stopping distribution by the PC5,6 cut

The PC5,6 cut that suppresses out of target stops changes the shape of the muon stopping distribution for the accepted event sample, see Fig. 2 in Sec. IV A. The effect of the cut depends on the resolution of the cut variable, which is the

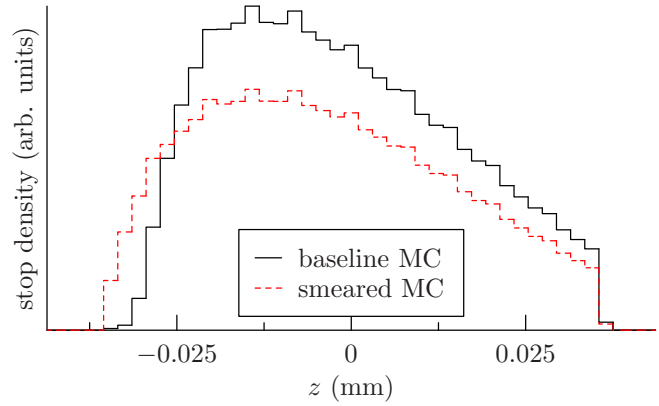

FIG. 8. Simulated distribution of muons stopping in the Al target for the baseline and smeared simulation after the PC5,6 cut.

time over threshold measurement in the wire chambers. A comparison of time over threshold spectra for data and MC showed that simulated distributions were sharper than data. To evaluate the corresponding systematic effect, time over threshold values were smeared in simulated samples to make MC shapes match those in data, and full analysis chain redone with the smearing applied. The effect of the smearing on the muon stopping distribution is shown in Fig. 8. We treat the difference between unfolding results for the baseline and smeared analyses as the systematic uncertainty corresponding to the chamber hit time over threshold modeling.

C. Crosstalk

The dominant crosstalk mechanism in the TWIST setup, identified by signal injection during bench tests of the detector, is that a real pulse on a sense wire induces an opposite polarity signal on neighboring wires. The opposite polarity pulse itself is not registered, but an overshoot after channel return to baseline sometimes crosses the discriminator threshold and is recorded as a delayed narrow pulse. Crosstalk was a minor effect for minimum ionizing positron tracks from muon decay [10], and was not implemented in the simulation. Instead, an algorithm to flag crosstalk hits in data based on their relative timing and time over threshold width was developed. Hits flagged as crosstalk were ignored by track reconstruction. Crosstalk is more important for heavily ionizing proton and deuteron tracks. For example, the mass stopping power $-dE/dx$ of dry air for a 50 MeV/c electron is 3.5 MeV cm^2/g [44], while for a 100 MeV/c proton it is 66 MeV cm^2/g, and it peaks above 700 MeV cm^2/g as the proton slows down [45]. This causes a much larger ionization density for proton tracks, leading to larger amplitude electric signals and more crosstalk hits.

To evaluate crosstalk effect in the present analysis, data reconstruction and unfolding were redone after unflagging at random a fraction of identified crosstalk hits. An increased amount of crosstalk at tracking input reduces the number of reconstructed tracks and changes the unfolded spectrum. This effect is linear in the unflagging fraction range from 0 to at least 0.1. Therefore the difference between the unfolding

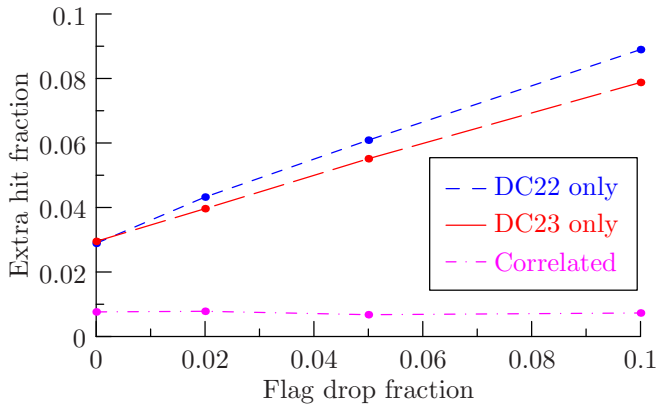

FIG. 9. Dependence of the observed correlated and uncorrelated extra hits in data on the crosstalk unflagging fraction.

result for an unflagging setting that doubles the amount of residual crosstalk hits and the baseline result provides an estimate of the systematic uncertainty caused by imperfect crosstalk removal: the true systematic of going from zero to one unit of cross talk is estimated by the measurable effect of increasing crosstalk from one to two units.

To determine the correct unflagging setting to measure the systematic, a sample of data events with positive tracks having $\theta < 40^\circ$ was analyzed for different configurations of hit wires in a DC plane. A single wire hit is attributed to a real signal from the track. Two adjacent wires may be due to two real or one real and one extra hit. A track with less than a 45° angle can not cause ionization in more than two square gas cells, therefore if more than two wires are hit there are extra hits in the plane. Also any configuration with nonadjacent hit wires must have extra hits. Some of the extra hits are crosstalk, while others are produced by extra particles in the event (such as a δ electron from the proton track). An extra particle can produce hits in multiple planes, while crosstalk hits in different planes are not correlated. This allows us to disentangle the two effects. Figure 9 shows observed rates of correlated and uncorrelated hits in DC22,23. As is expected, the rate of correlated hits does not change with the unflagging fraction setting, while the rate of uncorrelated hits grows linearly, confirming their crosstalk origin. The baseline rate of uncorrelated extra hits doubles for the unflagging fraction of 0.05, therefore this setting was used to determine the crosstalk systematic uncertainty.

D. Charged particle energy loss in detector material

This analysis relies on the modeling of proton and deuteron energy loss in material by out-of-the-box GEANT 3.21 [28]. The discussion in section PHYS430 of the GEANT manual suggests that the model is accurate to a few percent for low-energy protons. Reconstructed momentum spectra of contained tracks in our setup provide an experimental handle on the quality of the energy loss model. There is a visible discrepancy between data and simulation in the position of the momentum distribution peak for protons ranging out deep in the detector, see Fig. 6(e). The most probable momentum in data is 92.4 MeV/c while in MC it is 88.7 MeV/c. The about 4% difference is consistent with the expected accuracy of the simulation.

To evaluate the impact of the discrepancy on the final result, various changes to the simulation code have been tried. The original GEANT 3 computed energy loss for protons was scaled by velocity-dependent factors. In other simulation runs the amount of material in various parts of the detector was varied. While some of the variations improved data-MC agreement for contained tracks with long range, most of them broke the agreement for shorter contained or uncontained tracks. The variation that showed the best improvement for long contained tracks without introducing discrepancies in other regions was a 20% increase in the density of the drift chamber DME gas. This does not correspond to a realistic density uncertainty in the setup, but was used as a fudge factor to estimate the systematic effect of the energy loss modeling. Because the increased gas density also affects the muon stopping distribution, the muon beam momentum in the simulation was adjusted to mostly compensate for the change. A small correction compensating for a residual shift of the muon stopping distribution was applied to the difference between unfolding results with the modified simulation and the baseline to obtain the final estimate of the systematic uncertainty.

E. Heavy particle background simulation

The data unfolding fit included triton and α particles from the nuclear capture as a single background component with fixed shape and floating normalization. The shapes of triton and α distributions and their relative yields for the baseline fit were taken from the GEANT 4 precompound model as described in Sec. III. The Bertini cascade as implemented in GEANT 4 [33] provided an alternative model for the heavy particle spectra. The difference between the models is illustrated in Fig. 10. The systematic uncertainty was estimated as the difference between the unfolding results when using baseline and alternative inputs for the heavy particle background.

Protons are well separated from heavier particles by track range and momentum, so the proton yield is only weakly affected by the modeling of triton and α emissions, as can be seen in Table I. The deuteron result, on the other hand, is directly influenced by simulation of this background.

F. Unfolding procedure

The proton and deuteron spectra are approximated by cubic splines. To estimate the systematic uncertainty resulting from such approximation, the unfolding procedure was redone after increasing the number of splines in the basis set by one for protons or deuterons, one variation at a time. The variation of the proton parametrization changed the measured partial yield by 0.00028 for protons and 0.00022 for deuterons. The variation of the deuteron parameterization produced a 0.00012 change in the proton result and 0.00013 in the deuteron one.

The regularization term in the unfolding procedure biases the result. To estimate the bias, Tikhonov regularization term was used instead of the default MaxEnt form. This resulted in

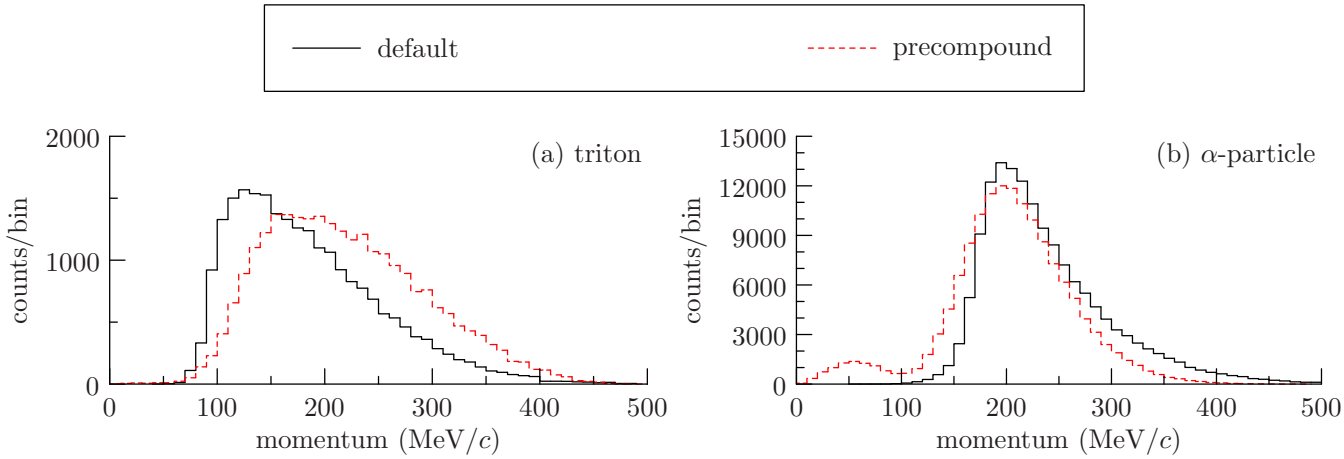

FIG. 10. Generator level triton and α particle momentum spectra for 10^7 muon nuclear captures on aluminum simulated with GEANT 4 precompound and Bertini models.

a 0.00008 change in the proton yield and 0.00005 change in the deuteron yield.

The quadratic sum of the parameterization and regularization effects is shown in Table I in the "Unfolding procedure" row.

G. Other effects

Deuteron breakup in detector material is a potential source of systematic uncertainty. A dedicated MC using cross sections from Refs. [46,47] showed that the fraction of deuterons breaking up in the detector was at the level of 10^{-3}, and thus negligible.

The background from DIO electrons misreconstructed as positive charge tracks is included in the fit. It contributes only at lowest momenta and contributes negligible uncertainty to the measured spectra. The geometry of the detector and the spectrometer magnetic field are known to a high accuracy [26,27], making the uncertainty due to momentum scale calibration negligible.

The proton and deuteron spectra are normalized per muon capture as described in Sec. IV D. The uncertainties due to the knowledge of the DIO spectrum and the data sample size have a negligible effect on the final result.

VI. RESULTS

Figures 11 and 12 show the differential yields of protons and deuterons per muon capture $f_{\text{proton}}(p)$ and $f_{\text{deuteron}}(p)$. As described in Sec. IV E, the unfolding splines are defined in the 80–230 MeV/c range for protons, and 130–200 MeV/c for deuterons. The higher momentum data included in the fit assume exponential (in kinetic energy) behavior, so there is no explicit upper cutoff for the fit range. We define an effective upper cutoff for this measurement as the momentum beyond which the expected contribution of the exponential tail to the reconstructed spectrum equals one event. This cutoff is

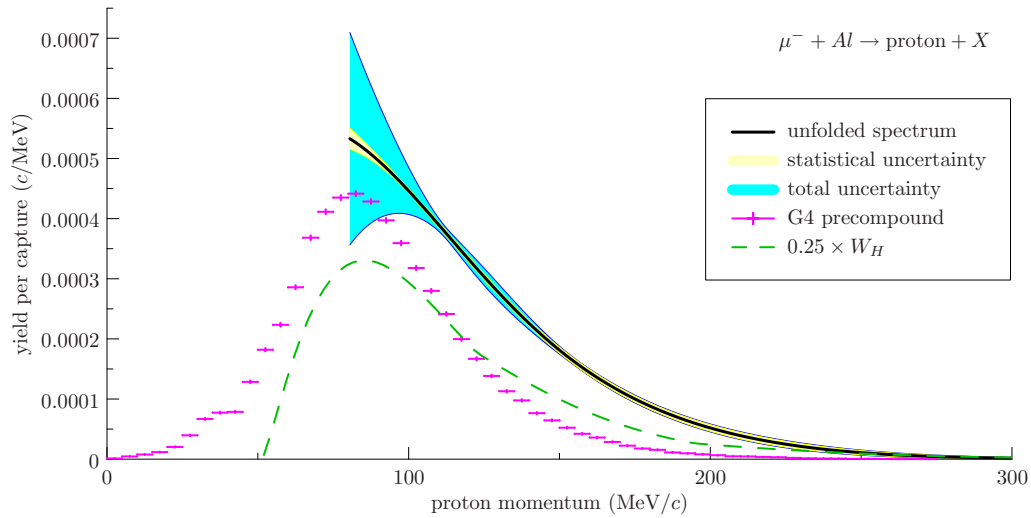

FIG. 11. Yield of protons per muon capture vs momentum.

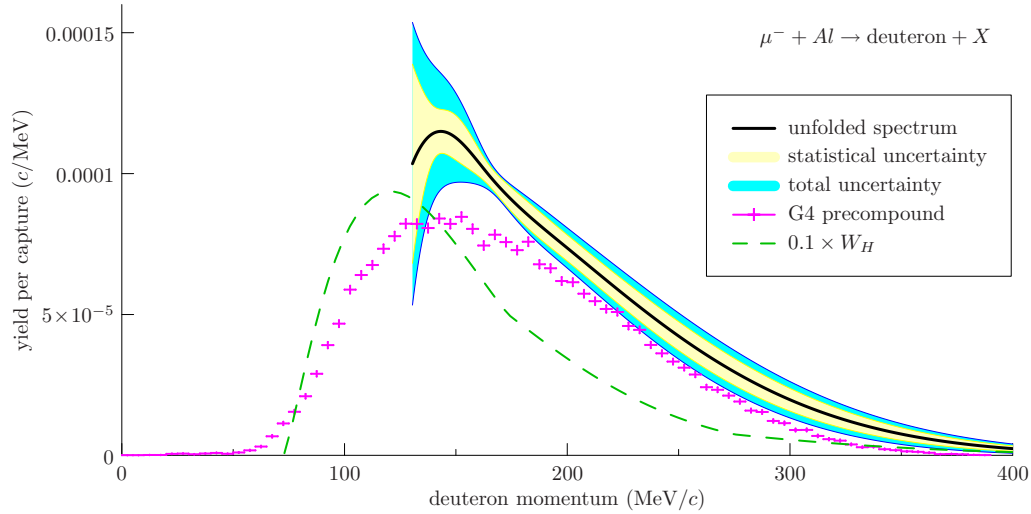

FIG. 12. Yield of deuterons per muon capture vs momentum.

about 300 MeV/c for protons and 400 MeV/c for deuterons. The uncertainty on the proton spectrum below 150 MeV/c is mostly systematic, while above 150 MeV/c it is dominated by the data sample statistics. The uncertainty band increase at the low momentum cutoff is due to crosstalk, which has a larger effect for short tracks with fewer hits. For deuteron the statistical and systematic contributions are of similar size in most of the range.

The dashed curves in Figs. 11 and 12 show the spectrum from Ref. [23], labeled as W_H, which is scaled by the arbitrary factors 0.25 and 0.1 for presentation purposes. The unscaled curve would dominate the plots. The figures also show the spectra predicted by GEANT 4 version 10.2p03 with the precompound model, as detailed in Sec. III. (The default codes for muon capture are in poor agreement with our data and are not shown.)

Integrating the unfolded spectra while taking into account bin-to-bin correlations, we obtain the per capture yields of

$$0.0322 \pm 0.0007(\text{stat}) \pm 0.0022(\text{syst}) \quad (2)$$

for protons above 80 MeV/c and

$$0.0122 \pm 0.0009(\text{stat}) \pm 0.0006(\text{syst}) \quad (3)$$

for deuterons above 130 MeV/c. The correlation coefficient between the visible yields, including all statistical and systematic uncertainties, is -0.25.

To extrapolate to the total yield we normalize the GEANT 4 precompound or W_H prediction to match our measured

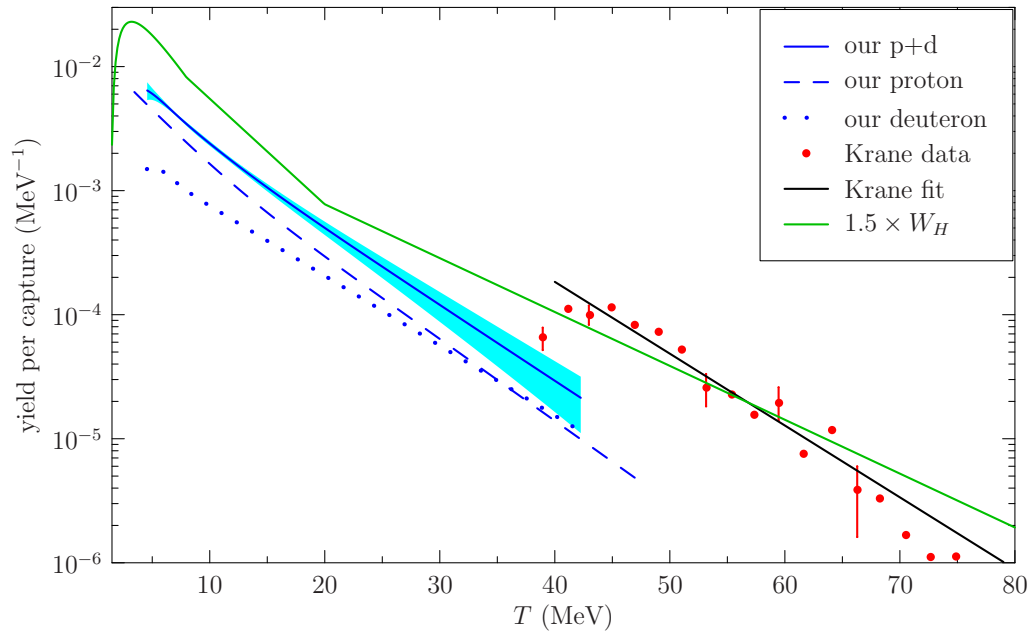

FIG. 13. Yield of charged particles per muon capture vs kinetic energy.

spectrum just above the threshold, and add the integrated yield up to our threshold to the measured yield. We take the average between GEANT 4 precompound and W_H results as the central value, and include half the difference in the extrapolation uncertainty. Another, smaller, contribution to the extrapolation uncertainty is obtained by varying the matching momentum. The resulting extrapolated total per capture yields are

$$0.045 \pm 0.001(\text{stat}) \pm 0.003(\text{syst}) \pm 0.001(\text{extrap}) \quad (4)$$

for protons and

$$0.018 \pm 0.001(\text{stat}) \pm 0.001(\text{syst}) \pm 0.002(\text{extrap}) \quad (5)$$

for deuterons. These numbers can be compared to the 2:1 ratio assumed in Ref. [23] and are close to the corresponding theoretical predictions of 0.040 and 0.012 [13]. Radioisotope yields for muon capture on aluminum are reported in Refs. [21,22] as 0.028 ± 0.004 for the final state consistent with (pn) emission, and 0.035 ± 0.008 for $(p2n)$. Note that the activation measurement technique can not distinguish separate p and n particles from a deuteron. The sum of the earlier measurements 0.063 ± 0.009 compares well to our sum of extrapolated proton and deuteron yields of 0.062 ± 0.004.

A measurement of the energy spectrum of charged particles from muon capture on aluminum above 40 MeV is reported in Ref. [20]. Figure 13 reproduces data points and the fit from that paper, along with our proton and deuteron results converted to kinetic energy spectra. While the slope of the fit in Ref. [20] agrees with that of our $p + d$ curve, the previously reported yield around 40 MeV is significantly higher. Figure 13 also reflects that a conservative normalization was taken for the W_H spectrum in Ref. [23]. The factor of 1.5 in the figure accounts for $1 \times W_H$ representing proton and $0.5 \times W_H$ deuteron contributions in that analysis.

VII. SUMMARY

The TWIST data taken with a μ^- beam incident on Al have been analysed for positive charged particles from muon capture. The detector was sensitive to protons with momentum above 80 MeV/c and deuterons above 130 MeV/c. These ranges are found to contain about 70% of the yield for each particle. A precision of better than 10% over the momentum range of 100–190 MeV/c for protons is obtained; for deuterons of 145–250 MeV/c the precision is better than 20%. The results are presented in a format suitable for building an event generator for use in simulations. They have immediate application to the design of experiments searching for μ to e conversion. These spectra are of interest as input to an improved theoretical understanding of the physics of muon capture on nuclei. They are strongly selective of the GEANT 4 precompound model over the other presented choices. The total per capture yields of 0.045 ± 0.003 for protons and 0.018 ± 0.002 for deuterons are the most precise measurements of these quantities to date.

ACKNOWLEDGMENTS

We thank all TWIST collaborators who contributed to detector construction and data taking, as well as TRIUMF staff. We thank Konstantin Olchanski who promptly fixed any computer problems we had. This work was supported in part by the Natural Sciences and Engineering Research Council of Canada, the Russian Ministry of Science, and the U.S. Department of Energy. One of the authors (A.G.) was supported by the resources of the Fermi National Accelerator Laboratory (Fermilab), a U.S. Department of Energy, Office of Science, HEP User Facility. Fermilab is managed by Fermi Research Alliance, LLC (FRA), acting under Contract No. DE-AC02-07CH11359.

APPENDIX: UNFOLDING PROCEDURE

As outlined in Sec. IV E, we use unfolding to determine truth level momentum spectra $f_\eta(p)$ ($\eta = \{\text{proton, deuteron}\}$) from the experimentally measured distribution of tracks in momentum and range. The data observables are the bin contents d_i in the exclusive channels (contained and uncontained), where reconstructed bin index i runs over all bins in the range vs momentum contained and momentum spectrum uncontained histograms. The detector response $R_{\eta,i}(p)$ is the expectation value of the number of reconstructed events in bin i for a single proton (or deuteron) emitted in the nuclear capture in the target with true momentum p. It describes all the detector effects: acceptance, efficiency, and resolution, but is independent of the physics spectra that are being measured. In practice, the detector response is approximated by a matrix $R_{\eta,ij}$ obtained by binning the true momentum variable axis: $\int R_{\eta,i}(p) f_\eta(p)\, dp \longrightarrow \sum_j R_{\eta,ij} f_{\eta,j}$. The response matrix $R_{\eta,ij}$ is determined from Monte Carlo simulation. If the bin size for the true momentum variable is much smaller than the momentum resolution, the result does not depend on a particular momentum spectrum used in the simulation—the only requirement is that the simulation reaches sufficient statistics in all of the phase space important for the measurement. This study used 1 MeV/c true momentum bin size.

The expected values of the data observables are written as

$$\mu_i = N_{\text{captures}} \sum_\eta \sum_j R_{\eta,ij} f_{\eta,j} + b_i, \quad (A1)$$

where b_i represent the background. Because many bins in the data sample contain only a few entries, the Poisson statistics must be taken into account. A maximum likelihood estimator for $f_{\eta,j}$ could be formed by maximizing

$$\log \mathcal{L}(d|\mu\{f\}) = \sum_i (d_i \log \mu_i - \mu_i) \quad (A2)$$

for the measured set of d_i. However, the unfolding problem is known to be ill posed [36–39]. The best possible unbiased solution of an unfolding problem would have an unacceptably large variance even if that solution saturated the minimal variance bound [37]. It has been shown that approximate solutions to unfolding problems can be obtained by using a regularization procedure [40–42], which reduces the variance of the result at the price of introducing a bias. Regularized unfolding can be performed by maximizing a combination of the log likelihood of data and a regularization functional $S\{f_\eta\}$

$$\mathcal{F} = \log \mathcal{L}(d|\mu\{f\}) + \alpha S\{f\}, \quad (A3)$$

where α is the regularization parameter. A widely used Tikhonov regularization imposes a smoothness requirement on the spectrum by penalizing the second derivative of the solution:

$$S_{\text{Tikhonov}} = -\sum_{\eta}\sum_{j}(-f_{\eta,j} + 2f_{\eta,j+1} - f_{\eta,j+2})^2. \quad \text{(A4)}$$

It therefore biases the result towards a linear function. Another well-established regularization, the maximum entropy (or MaxEnt) approach [37], is based on the entropy of a probability distribution [48]:

$$S_{\text{MaxEnt}} = -\sum_{\eta}\sum_{j} q_{\eta,j}\ln(q_{\eta,j}), \quad q_{\eta,j} \equiv f_{\eta,j}/\sum_{k} f_{\eta,k}. \quad \text{(A5)}$$

It biases the result towards a constant. A useful feature of the MaxEnt approach is that it guarantees that the result will be positive everywhere, as is required for particle emission spectra.

One can represent f_η in Eq. (A1) with cubic splines, as is conventionally done [36], and proceed with the regularized fit. However, as explained in Sec. IV E, spectra extracted in that way in our case are not physically plausible because of artifacts of the unfolding. A better result is obtained by following a modified unfolding method explained in Ref. [43], which adds more problem-specific physical information to the generic mathematical apparatus of unfolding. In this approach $f_\eta(p)$ are arbitrary functions below an unfolding cutoff, and physically motivated exponentials in kinetic energy above the cutoff, with parameters of the exponents included in the fit. The continuation of the solution with a parametrized function outside of the unfolding region provides a correct handling of the overflow region contribution. Another key idea is to impose regularization not on the complete physics spectrum, but on just the arbitrary function part of it, with the overall exponential behavior factored out. Then a regularization term that biases its spectrum to a constant will bias the final physics spectrum towards the exponential shape, without pulling up the low statistics tail. Specifically, we represent

$$f_\eta(p) = A_\eta \frac{p}{\sqrt{p^2 + m_\eta^2 c^2}} \exp\{-\gamma_\eta T_\eta(p)\} \times \begin{cases} 1 + \phi_\eta(p) & \text{for } p_{\eta,\min} < p \leqslant p_{\eta,u}, \\ 1 & \text{for } p > p_{\eta,u}, \end{cases} \quad \text{(A6)}$$

where $p_{\eta,\min}$ and $p_{\eta,u}$ specify the limits of the unfolding region for particle type η, m_η is the mass of the particle and $T_\eta(p)$ its kinetic energy, A_η and γ_η are parameters pertaining to the exponential behavior of the spectrum, and $\phi_\eta(p)$ is an arbitrary function to be determined from the unfolding. The regularization term has the form (A4) or (A5) but now acts on $1 + \phi$ instead of f:

$$\tilde{S}_{\text{Tikhonov}} = -\sum_{\eta}\sum_{j}(-\phi_{\eta,j} + 2\phi_{\eta,j+1} - \phi_{\eta,j+2})^2, \quad \text{(A7)}$$

$$\tilde{S}_{\text{MaxEnt}} = -\sum_{\eta}\sum_{j}\tilde{q}_{\eta,j}\ln(\tilde{q}_{\eta,j}),$$

$$\tilde{q}_{\eta,j} \equiv (1 + \phi_{\eta,j})/\sum_{k}(1 + \phi_{\eta,k}). \quad \text{(A8)}$$

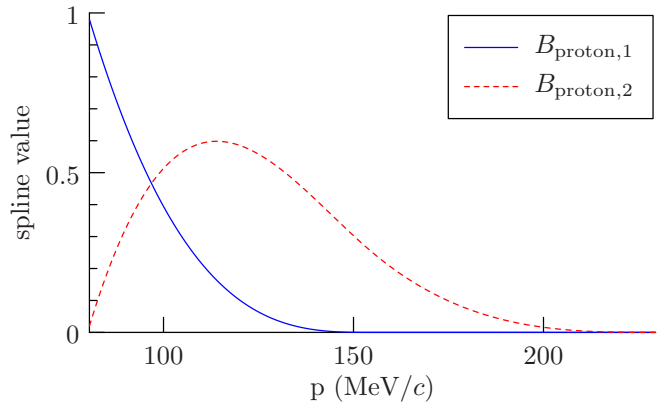

FIG. 14. Basis splines for the proton spectrum.

We used the MaxEnt term to extract the central value and most systematic uncertainties, and Tikhonov term to evaluate the uncertainty related to the regularization itself.

The functions ϕ_η are approximated by linear combinations of cubic basis splines B_l (B splines) [49] on their unfolding intervals

$$\phi_\eta(p) = \sum_{l}^{n_\eta} w_{\eta,l} B_{\eta,l}(p), \quad p_{\eta,\min} < p \leqslant p_{\eta,u}. \quad \text{(A9)}$$

Here $w_{\eta,l}$ are the spline coefficients determined from the unfolding process. We require that the resulting spectrum has a continuous second derivative, or $\phi_\eta(p_{\eta,u}) = \phi'_\eta(p_{\eta,u}) = \phi''_\eta(p_{\eta,u}) = 0$, which is provided by having a single-fold spline knot at the endpoint $p_{\eta,u}$. There are no continuity constraints at $p_{\eta,\min}$, therefore a fourfold knot is used at that point to support the most general cubic spline shape.

The values $p_{\text{proton},\min} = 80$ MeV/c and $p_{\text{deuteron},\min} = 130$ MeV/c are set by the turn-on of the respective acceptance times efficiency curves, see Fig. 4. The transition point between unfolding and exponential fit regions $p_{\text{proton},u} = 230$ MeV/c and $p_{\text{deuteron},u} = 200$ MeV/c, as well as the number and position of intermediate knots, were optimized based on unfolding of multiple, statistically independent mixed samples of simulated protons, deuterons, and the backgrounds. The mixed samples were designed to have statistics similar to the statistics of the actual data sample. The final choice of splines for the proton spectrum is defined by the sequence

TABLE II. Parameters of the unfolded spectra, defined in Eqs. (A6) and (A9).

Parameter	Value	Uncertainty
A_{proton} (c/MeV)	6.0×10^{-3}	2.4×10^{-3}
γ_{proton} (MeV^{-1})	1.5×10^{-1}	2.2×10^{-2}
$w_{\text{proton},1}$	7.4×10^{-1}	6.8×10^{-1}
$w_{\text{proton},2}$	5.1×10^{-1}	5.5×10^{-1}
A_{deuteron} (c/MeV)	2.7×10^{-3}	5.9×10^{-4}
γ_{deuteron} (MeV^{-1})	1.3×10^{-1}	2.1×10^{-2}
$w_{\text{deuteron},1}$	-3.6×10^{-2}	4.5×10^{-1}
$w_{\text{deuteron},2}$	2.1×10^{-1}	3.5×10^{-1}

TABLE III. Correlation between parameters of the unfolded spectra.

	A_{proton}	γ_{proton}	$w_{\text{proton},1}$	$w_{\text{proton},2}$	A_{deuteron}	γ_{deuteron}	$w_{\text{deuteron},1}$	$w_{\text{deuteron},2}$
A_{proton}	1.00	0.96	−0.48	−0.84	−0.14	−0.26	−0.03	−0.21
γ_{proton}		1.00	−0.64	−0.76	−0.26	−0.39	−0.05	−0.24
$w_{\text{proton},1}$			1.00	0.06	0.48	0.63	0.28	0.34
$w_{\text{proton},2}$				1.00	0.09	0.07	−0.15	−0.10
A_{deuteron}					1.00	0.90	0.23	−0.36
γ_{deuteron}						1.00	0.32	−0.01
$w_{\text{deuteron},1}$							1.00	−0.04
$w_{\text{deuteron},2}$								1.00

of knots 80, 80, 80, 80, 155, 230 MeV/c, resulting in a set of two basis functions that are illustrated in Fig. 14. The deuteron spline sequence is 130, 130, 130, 130, 165, 200 MeV/c, similarly resulting in two cubic splines.

One may notice that particle ID information is lacking for protons above 120 MeV/c, where the acceptance for the contained sample shown in Fig. 4 vanishes. To understand why it is possible to extend the proton unfolding region up to 230 MeV/c, one can consider deuterons first. Particle ID for deuterons is available in their full unfolding range 130–200 MeV/c. The shape of the deuteron spectrum is constrained from data in this range, and assumed to be exponential for higher momenta. Once the deuteron spectrum is determined, the rest of reconstructed data entries are attributed to protons and a small fixed shape background. Therefore unfolding range for protons does not have to match their particle ID acceptance region.

Background b_i in Eq. (A1) was represented as

$$b_i = b_{h,i} + b_{e,i} = \beta_h \frac{b^{\text{MC}}_{h,i}}{\sum_j b^{\text{MC}}_{h,j}} + \beta_e \frac{b^{\text{MC}}_{e,i}}{\sum_j b^{\text{MC}}_{e,j}}.$$

where b_h included all heavier than deuteron particles contributing to the reconstructed spectrum, and b_e accounted for DIO electrons misreconstructed as positive tracks. The shape of each background was taken from the simulation described in Sec. III, and the normalizations β_h and β_e were free fit parameters.

The regularization strength α in Eq. (A3) should be chosen to provide an optimal balance between the variance and the bias of the result. The method used in this study was inspired by the L-curve approach [50,51], and is the following. For a given α the maximization of $\tilde{\mathcal{F}} = \log \mathcal{L} + \alpha \tilde{S}$ yields particular values of $\log \mathcal{L}$ and $\tilde{S}$. We consider a parametric curve $(\log\log \mathcal{L}(\alpha), \log|\tilde{S}(\alpha)|)$, and use the α corresponding to the point of the maximum curvature of that curve as the optimal solution. This choice of L-curve variables for the log-likelihood fit and Tikhonov regularization corresponds to the classical L curve defined for a χ^2 unfolding [50]. For the MaxEnt regularization we explored several functions of $\tilde{S}$ and chose $\log|\tilde{S}|$ based on the tests with Monte Carlo samples.

Both data and simulation sample sizes contribute to the statistical uncertainty of the result. To estimate the data contribution, the central values of $f_{\text{proton}}(p)$, $f_{\text{deuteron}}(p)$, and the backgrounds were determined first by performing unfolding on the actual data sample. Those values were used to calculate expectation values for each data bin μ_i using Eq. (A1). Then pseudodata contained and uncontained histograms were produced by sampling an appropriate Poisson distribution for each bin, and the whole unfolding procedure, including a new choice of the optimal α, was performed on that pseudodata sample. The procedure was repeated for 25 statistically independent pseudodata samples, and the variance of f_η was computed from pseudodata unfolding results. The contribution of simulation statistics was estimated by splitting a simulation sample into parts and performing unfolding on real data using only one part of that MC sample at a time, and looking at the variation of the result. The sizes of MC samples were confirmed to be sufficiently large, so that the statistical uncertainty of the result is dominated by the real data statistics.

The unfolded proton and deuteron spectra are shown in Figs. 11 and 12, their parameters are summarized in Table II, and correlations in Table III. The uncertainties shown in Table II include statistical and most systematic contributions described in Sec. V. The parametrization shape uncertainty is not representable in terms of the fixed set of fit parameters, and is the only contribution that is not included.

[1] P. Haff and T. Tombrello, Negative muon capture in very light atoms, Ann. Phys. (NY) **86**, 178 (1974).
[2] P. Vogel *et al.*, Muon capture in atoms, crystals and molecules, Nucl. Phys. A **254**, 445 (1975).
[3] D. Measday, The nuclear physics of muon capture, Phys. Rep. **354**, 243 (2001).
[4] J. Nieves, J. E. Amaro, and M. Valverde, Inclusive quasielastic charged-current neutrino-nucleus reactions, Phys. Rev. C **70**, 055503 (2004); **72**, 019902(E) (2005).
[5] J. Nieves, I. R. Simo, and M. J. Vicente Vacas, Inclusive charged-current neutrino-nucleus reactions, Phys. Rev. C **83**, 045501 (2011).

[6] L. Bartoszek *et al.* (Mu2e Collaboration), Mu2e Technical Design Report, FERMILAB-TM-2594, FERMILAB-DESIGN-2014-01, 2014, arXiv:1501.05241 [physics.ins-det].

[7] Y. Kuno (COMET Collaboration), A search for muon-to-electron conversion at J-PARC: The COMET experiment, Prog. Theor. Exp. Phys. **2013**, 022C01 (2013).

[8] R. P. Litchfield (AlCap Collaboration), Status of the AlCap experiment, in *Proceedings of the 16th International Workshop on Neutrino Factories and Future Neutrino Beam Facilities (NUFACT 2014): Glasgow, Scotland, UK, 25–30 August 2014*, PoS **NUFACT2014**, 095 (2015).

[9] N. L. Rodning *et al.* (TWIST Collaboation), TWIST - The TRIUMF Weak Interaction Symmetry Test: The Michel parameters from mu+ decay, *Tau lepton physics. Proceedings of the 6th International Workshop, TAU 2000, Victoria, Canada, September 18-21, 2000*, Nucl. Phys. Proc. Suppl. **98**, 247 (2001).

[10] A. Hillairet, R. Bayes, J. F. Bueno, Y. I. Davydov, P. Depommier, W. Faszer, C. A. Gagliardi, A. Gaponenko, D. R. Gill *et al.* (TWIST Collaboration), Precision muon decay measurements and improved constraints on the weak interaction, Phys. Rev. D **85**, 092013 (2012).

[11] A. Grossheim, R. Bayes, J. F. Bueno, P. Depommier, W. Faszer, M. C. Fujiwara, C. A. Gagliardi, D. R. Gill, P. Gumplinger *et al.* (TWIST Collaboration), Decay of negative muons bound in ^{27}Al, Phys. Rev. D **80**, 052012 (2009).

[12] M. Lifshitz and P. Singer, Charged Particle Emission Following Muon Capture in Complex Nuclei, Phys. Rev. Lett **41**, 18 (1978).

[13] M. Lifshitz and P. Singer, Nuclear excitation function and particle emission from complex nuclei following mu capture, Phys. Rev. C **22**, 2135 (1980).

[14] M. Lifshitz and P. Singer, Meson exchange currents and energetic particle emission from μ^- capture, Nucl. Phys. A **476**, 684 (1988).

[15] H. Morinaga and W. Fry, Nuclear capture of negative μ mesons in photographic emulstions, Nuovo Cimento Ser. 9 **10**, 308 (1953).

[16] D. Kotelchuck and J. V. Tyler, Search for a conserved-vector-current mechanism in the emission of protons from μ^- stars in emulsion, Phys. Rev. **165**, 1190 (1968).

[17] A. O. Vaisenberg, E. D. Kolganova, and N. V. Rabin, High energy protons in the absorbtion of muons by emulsion nuclei, Sov. J. Nuc. Phys. **11**, 464 (1970).

[18] S. E. Sobottka and E. L. Wills, Energy Spectrum of Charged Particles Emitted Following Muon Capture in Si^{28}, Phys. Rev. Lett. **20**, 596 (1968).

[19] Yu. G. Budyashov, V. G. Zinov, A. D. Konin, A. I. Mukhin, and A. M. Chatrchyan, Charged particles from the capture of negative muons by the nuclei ^{28}Si, ^{32}S, ^{40}Ca, and ^{64}Cu, Sov. Phys. JETP **33**, 11 (1971) [Zh. Eksp. Teor. Fiz. **60**, 19 (1971)].

[20] K. S. Krane, T. C. Sharma, L. W. Swenson, D. K. McDaniels, P. Varghese, B. E. Wood, R. R. Silbar, H. D. Wohlfahrt, and C. A. Goulding, Energetic charged-particle spectrum following μ^- capture by nuclei, Phys. Rev. C **20**, 1873 (1979).

[21] A. Wyttenbach, P. Baertschi, S. Bajo, J. Hadermann, K. Junker *et al.*, Probabilities of muon induced nuclear reactions involving charged particle emission, Nucl. Phys. A **294**, 278 (1978).

[22] G. Heusser and T. Kirsten, Radioisotope production rates by muon capture, Nucl. Phys. A **195**, 369 (1972).

[23] E. V. Hungerford, Comment on proton emission after muon capture, MECO Note 34 (1999), arXiv:1803.08403v1.

[24] M. Bachman *et al.*, A search for $\mu^- N \to e^- N$ with sensitivity below 10^{-16} (1996), AGS Letter of Intent.

[25] S. Agostinelli *et al.* (GEANT 4 Collaboration), GEANT 4: A Simulation toolkit, Nucl. Instrum. Meth. A **506**, 250 (2003).

[26] R. S. Henderson *et al.*, Precision planar drift chambers and cradle for the TWIST muon decay spectrometer, Nucl. Instrum. Meth. A **548**, 306 (2005).

[27] J. F. Bueno, R. Bayes, Y. I. Davydov, P. Depommier, W. Faszer, C. A. Gagliardi, A. Gaponenko, D. R. Gill, A. Grossheim *et al.* (TWIST Collaboration), Precise measurement of parity violation in polarized muon decay, Phys. Rev. D **84**, 032005 (2011); **85**, 039908(E) (2012).

[28] R. Brun, F. Bruyant, F. Carminati, S. Giani, M. Maire, A. McPherson, G. Patrick, and L. Urban, *GEANT: Detector Description and Simulation Tool; Oct 1994*, CERN Program Library (CERN, Geneva, 1993) Long writeup W5013, http://dx.doi.org/10.17181/CERN.MUHF.DMJ1.

[29] R. P. MacDonald, R. Bayes, J. Bueno, Y. I. Davydov, P. Depommier, W. Faszer, M. C. Fujiwara, C. A. Gagliardi, A. Gaponenko *et al.* (TWIST Collaboration), Precision measurement of the muon decay parameters ρ and δ, Phys. Rev. D **78**, 032010 (2008).

[30] J. Allison *et al.*, Recent developments in Geant4, Nucl. Instrum. Meth. A **835**, 186 (2016).

[31] J. Allison *et al.*, Geant4 developments and applications, IEEE Trans. Nucl. Sci. **53**, 270 (2006).

[32] J. M. Quesada *et al.*, Recent developments in pre-equilibrium and de-excitation models in GEANT4, Prog. Nucl. Sci. Tech. **2**, 936 (2011).

[33] D. H. Wright and M. H. Kelsey, The Geant4 Bertini Cascade, Nucl. Instrum. Meth. A **804**, 175 (2015).

[34] J. Bueno, A direct measurement of $P_\mu^\pi \xi$ from muon decay, Ph.D. thesis, The University of British Columbia, Vancouver, 2010.

[35] T. Suzuki, D. F. Measday, and J. P. Roalsvig, Total nuclear capture rates for negative muons, Phys. Rev. C **35**, 2212 (1987).

[36] V. Blobel, Unfolding Methods in High-energy Physics Experiments, in *Proceedings of the 8th CERN School of Computing, Aiguablava, Spain, September 9–22 1984* (CERN, Geneva, 1984).

[37] G. Cowan, *Statistical Data Analysis* (Clarendon Press, Oxford, 1998).

[38] G. Cowan, A survey of unfolding methods for particle physics, *Advanced Statistical Techniques in Particle Physics. Proceedings of the Conference, Durham, UK, March 18–22, 2002*, Conf. Proc. **C0203181**, 248 (2002).

[39] H. B. Prosper and L. Lyons, in *Proceedings of the PHYSTAT 2011 Workshop on Statistical Issues Related to Discovery Claims in Search Experiments and Unfolding, CERN,Geneva, Switzerland 17-20 January 2011*, CERN (CERN, Geneva, 2011).

[40] A. N. Tikhonov, Solution of incorrectly formulated problems and the regularization method, Soviet Mathematics Dokl. **4**, 1035 (1963).

[41] A. N. Tikhonov, Regularization of ill-posed problems, Soviet Mathematics Dokl. **4**, 1624 (1963).

[42] D. L. Phillips, A technique for the numerical solution of certain integral equations of the first kind, J. Assoc. Comput. Mach. **9**, 84 (1962).

[43] A. Gaponenko, A practical way to regularize unfolding of sharply varying spectra with low data statistics, Nucl. Instrum. Meth. A **960**, 163612 (2020).
[44] ICRU report 37, stopping powers for electrons and positrons (1984), interactive tables available from the NIST web site.
[45] ICRU report 49, stopping powers and ranges for protons and alpha particles (1993), interactive tables available from the NIST web site.
[46] A. Auce, R. F. Carlson, A. J. Cox, A. Ingemarsson, R. Johansson, P. U. Renberg, O. Sundberg, and G. Tibell, Reaction cross sections for 38, 65, and 97 MeV deuterons on targets from ^{9}Be to ^{208}Pb, Phys. Rev. C **53**, 2919 (1996).
[47] P. C. Huu-Tai, Systematic study of elastic and reaction cross sections of deuteron induced reactions within the CDCC approach, Nucl. Phys. A **773**, 56 (2006).
[48] C. E. Shannon, A mathematical theory of communication, Bell Syst. Tech. J. **27**, 379 (1948).
[49] C. d. Boor, *A Practical Guide to Splines* (Springer Verlag, New York, 1978).
[50] P. C. Hansen, Analysis of discrete ill-posed problems by means of the L-curve, SIAM Rev. **34**, 561 (1992).
[51] P. C. Hansen and D. P. O'Leary, The use of the L-curve in the regularization of discrete ill-posed problems, SIAM J. Sci. Comput. **14**, 1487 (1993).